ACS Partner Journal

CHEM & BIO ENGINEERING

pubs.acs.org/ChemBioEng

Article

Applying TiO_{2-x}-Based Electrocatalysis and Photoelectrocatalysis Induced I^-/IO_3^- Recycling for Green and Continuous Ozone Removal

Jiahong Liao, Wenyi Wang, Weicheng Tong, Lixia Qiu, Hao Cheng, Xinben Zhao, Yi He, Chunlin Yu,* and Xingwang Zhang*

Cite This: *Chem Bio Eng.* 2025, 2, 322−331

Read Online

ACCESS | Metrics & More | Article Recommendations | Supporting Information

ABSTRACT: Solution absorption is a straightforward and efficient method for ozone treatment, but waste from inactive absorption solutions poses a risk of secondary pollution and raises the operating cost. Therefore, developing a sustainable recycling process for the absorption solution is essential for green ozone removal. In this study, we constructed a novel I^-/IO_3^- cycling system induced by electrocatalysis and photoelectrocatalysis to facilitate the reduction of KIO_3 in KI/KOH ozone absorption solution, thereby enabling absorption solution recycling. The stable operation of this system relies on high-performance cathode materials. By adjusting the concentration of oxygen vacancies on TiO_2, we reduced the energy barrier for IO_3^- reduction, optimized IO_3^- adsorption on the electrode surface, and improved the band gap structure of the electrode material, resulting in a TiO_{2-x} cathode with good IO_3^- reduction reaction (IO_3RR) performance. Notably, this method achieves an ozone removal cost of $3.72 per kilogram, only one-third of the cost associated with conventional catalytic ozone decomposition. This approach provides a promising new direction for green and efficient ozone removal.

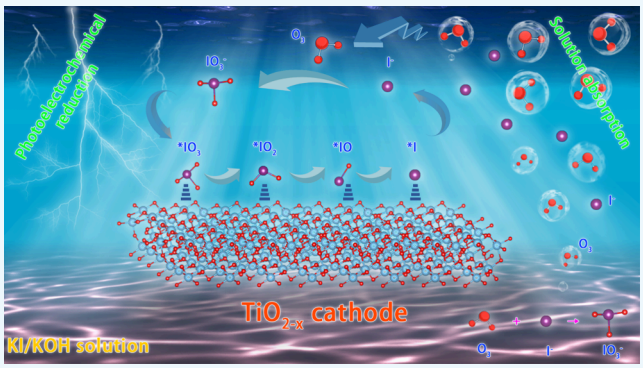

KEYWORDS: *Ozone removal, I^-/IO_3^-, TiO_{2-x}, Green chemical process, IO_3^- reduction reaction (IO_3RR)*

1. INTRODUCTION

Ozone is a prevalent air pollutant characterized by an irritating odor and strong oxidizing properties. Prolonged exposure to high concentrations of ozone gas can cause a range of respiratory and cardiopulmonary diseases. For this reason, the U.S. Environmental Protection Agency (EPA)[1] and the Ministry of Ecology and Environment of the People's Republic of China have established clear standards for minimum ground-level ozone concentrations.[2] Therefore, the effective removal of ozone gas holds great significance in terms of environmental protection and people's health.[3−5]

Currently, the most commonly used ozone treatment methods include thermal decomposition,[6] activated carbon adsorption,[7] catalytic decomposition,[8−11] and solution absorption.[12,13] Among them, thermal decomposition, which involves the conversion of ozone into oxygen at high temperatures, incurs significant operational expenses. The application of the activated carbon adsorption method is limited due to the generation of microwastes during its use. Currently, catalytic decomposition is considered the most promising ozone treatment method. However, the irreversible occupation of ozone decomposition intermediates and the high humidity of the ozone gas lead to rapid deactivation of the catalyst, which greatly increases the cost and limits the wide-scale application of this method.[9,10,14,15] The solution absorption method,[13,16] on the other hand, as a reactive ozone treatment technique offers ease of operation while delivering exceptional results in ozone removal. However, a large amount of waste liquid is generated by the failure of the absorbing solution, leading to significant secondary pollution. The green recycling of the absorbing solution is, therefore, crucial for the continuous and efficient removal of ozone.

KI absorption solution is extensively employed in the solution absorption method due to its exceptional efficacy in absorbing ozone. The national standard of the People's Republic of China, GB/T 37894-2019, also explicitly specifies the utilization of the iodometric method for determining the concentration of ozone in gas. Ozone, being a potent oxidizing agent, oxidizes KI to free I_2 monomers upon absorption by KI solutions (eq 1-1). However, under alkaline conditions, I_2 undergoes spontaneous disproportionation to form IO_3^- and I^- (eq 1-2). Therefore, the KI solution absorbs ozone and

Received: December 28, 2024
Revised: March 3, 2025
Accepted: March 7, 2025
Published: March 17, 2025

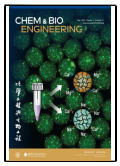

https://doi.org/10.1021/cbe.4c00187
Chem Bio Eng. 2025, 2, 322−331

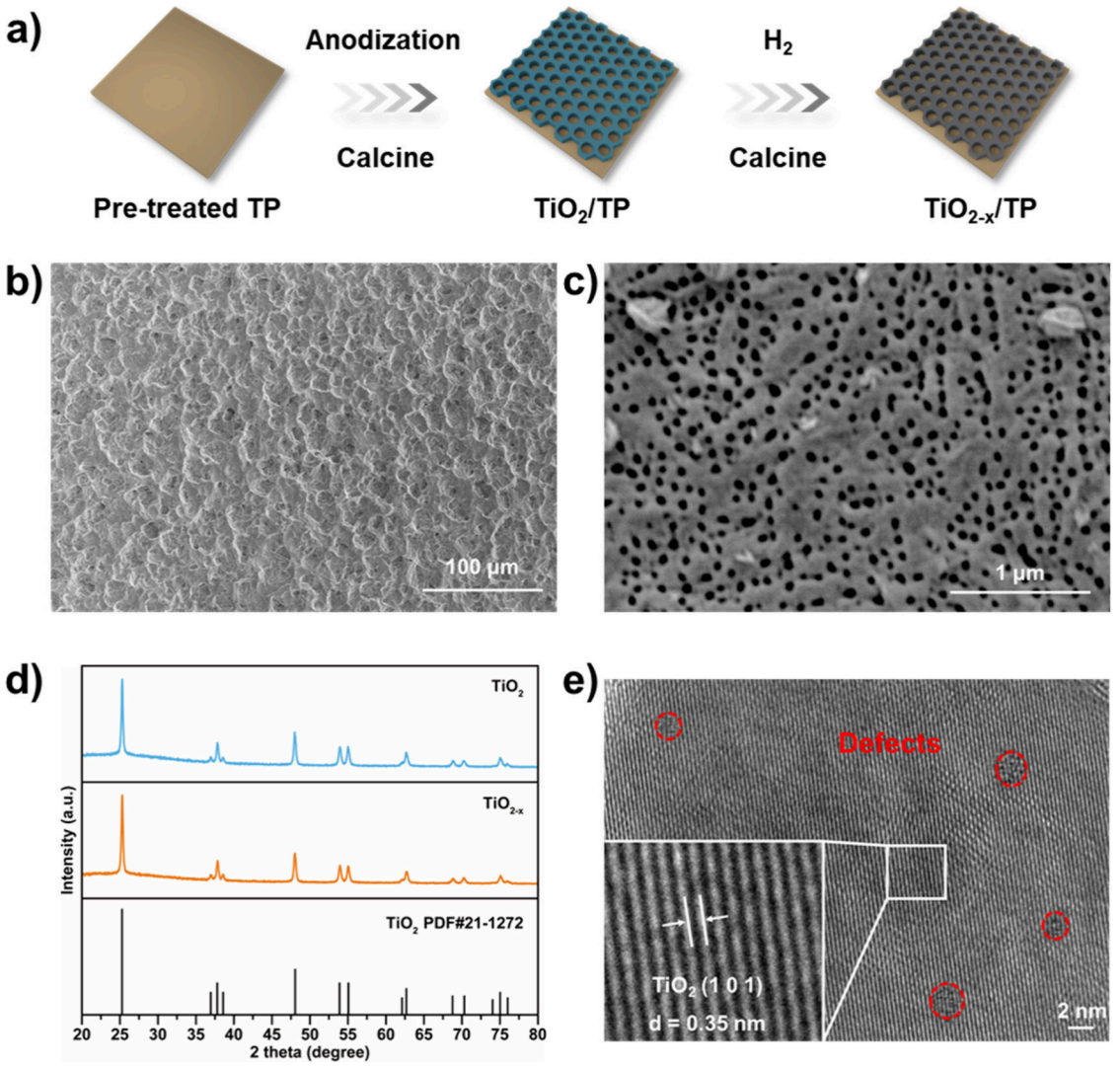

Figure 1. (a) Schematic diagram of TiO_{2-x}/TP synthesis, (b) SEM image of pretreated TP, (c) SEM image of TiO_2/TP surface, (d) XRD patterns of TiO_2 and TiO_{2-x}, and (e) HRTEM image of TiO_{2-x} (TiO_{2-x} calcination conditions: 500 °C for 4 h under a H_2 atmosphere).

eventually transforms into a KIO_3 solution (eq 1-3). Reducing KIO_3 to KI is crucial for the absorption solution cycle.

$$6I^- + O_3 + 3H_2O \rightarrow 3I_2 + 6OH^- \quad (1\text{-}1)$$

$$3I_2 + 6OH^- + \rightarrow IO_3^- + 5I^- + 3H_2O \quad (1\text{-}2)$$

$$I^- + O_3 \rightarrow IO_3^- \quad (1\text{-}3)$$

Electrochemical and photoelectrochemical processes, as representatives of green and sustainable processes, are characterized by high resource utilization and no waste emissions. Therefore, the electrochemical and photoelectrochemical reduction of KIO_3 is undoubtedly an excellent choice.[17−21] Among the many electrocatalytic and photoelectrocatalytic materials, TiO_2 electrodes are widely used due to their excellent catalytic properties and stable structures.[21−23] Additionally, defect engineering serves as a prevalent approach to enhance the performance of catalysts.[24,25] For example, Xu et al.[26] used the plasma technique to construct a large number of oxygen vacancies on the Co_3O_4 surface, which significantly enhanced the electrocatalytic activity of the sample. Consequently, defect-rich TiO_2 materials could be deemed as a favorable option for KIO_3 reduction.

In this paper, we synthesized a TiO_{2-x} cathode enriched with oxygen vacancies, using anodic oxidation combined with high-temperature calcination with hydrogen. The test results show that the TiO_{2-x} cathode, supported by a Ti plate (TiO_{2-x}/TP), exhibits extremely high electrocatalytic activity and achieves nearly 100% Faradaic efficiency in the KIO_3 reduction reaction (IO_3RR). The density functional theory (DFT) results show that the introduction of oxygen vacancies facilitated the adsorption of IO_3^- on the TiO_{2-x} electrode while simultaneously reducing the energy barrier for the IO_3^- reduction reaction, thereby greatly enhancing the electrocatalytic performance of IO_3RR. Besides, the TiO_{2-x}/TP cathode was applied to the I^-/IO_3^- system for ozone removal; the system maintained 100% ozone conversion after 30 days of operation. Furthermore, we investigated the potential of photoelectrochemical reduction in this system, and the experimental results show that the introduction of oxygen vacancies optimizes the band gap of TiO_2 and suppresses the recombination of electron−hole pairs, resulting in excellent photoelectrochemical properties of TiO_{2-x} loaded on fluorine-doped tin oxide (FTO) conductive glass substrates. These findings confirm the viability of using solar energy as a cycle-driven energy source for the system. The experimental results

https://doi.org/10.1021/cbe.4c00187
Chem Bio Eng. 2025, 2, 322−331

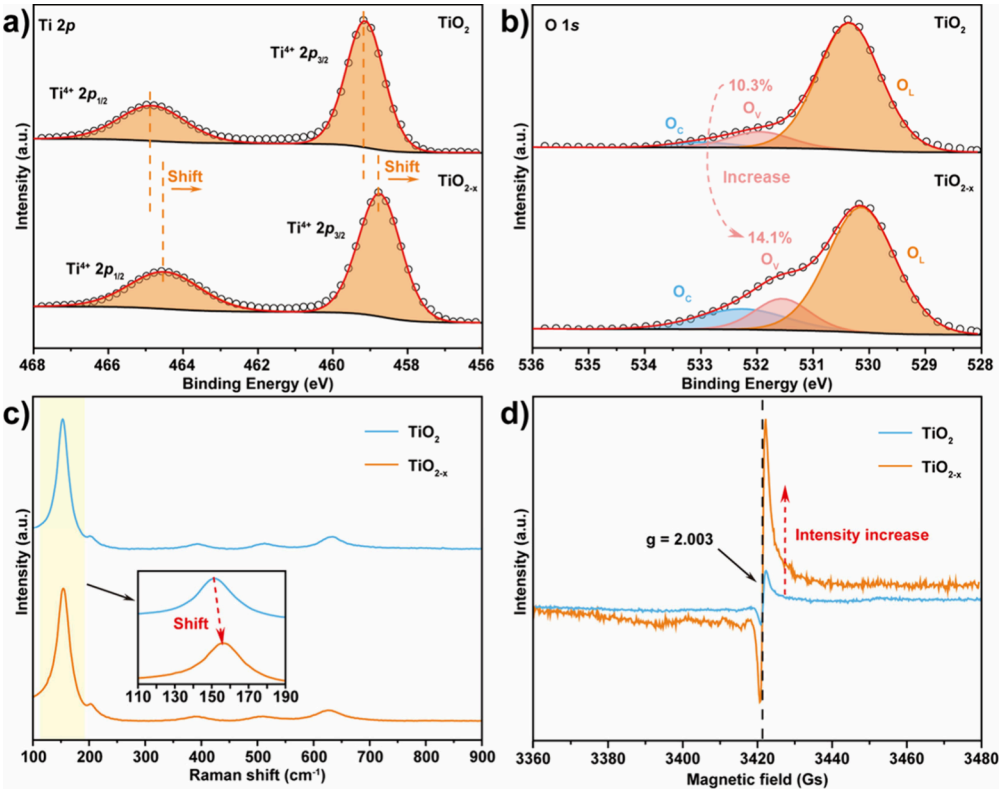

Figure 2. XPS spectra of TiO_2 and TiO_{2-x}: (a) Ti 2p and (b) O 1s. (c) Raman spectra of TiO_2 and TiO_{2-x}. (d) EPR spectra of TiO_2 and TiO_{2-x} (TiO_{2-x} calcination conditions: 500 °C for 4 h under a H_2 atmosphere).

described above greatly demonstrate the promising industrial application of this system for green and continuous ozone removal.

2. EXPERIMENTAL SECTION

2.1. Materials. Titanium plates were procured from Xi'an Taijin Industrial Electrochemical Technology Co., Ltd. Potassium iodide (KI) was sourced from Shanghai Macklin Biochemical Co., Ltd., while potassium hydroxide (KOH) was obtained from Sinopharm Chemical Reagent Co., Ltd. Fluorine-doped tin oxide (FTO) conductive glass substrates were supplied by Hangzhou Fei Shi Er Biotechnology Co., Ltd. All experiments utilized deionized water with a resistivity of 18.2 MΩ·cm.

2.2. Pretreatment of Titanium Plates. Titanium plates with a working area of 1.0 cm^2 served as substrates. Before use, the titanium plates underwent a pretreatment process. This involved sandblasting, followed by ultrasonic cleaning for 60 min in a 5 wt % sodium carbonate solution. Subsequently, the plates were etched for 2 h in a 20 wt % hydrochloric acid solution at 80 °C and finished with a 15 min ultrasonic cleaning in deionized water.

2.3. Synthesis of TiO_2/TP. The TiO_2 electrode, supported by a titanium plate (TiO_2/TP), was prepared through an electrochemical anodization process using a conventional two-electrode setup with the titanium plate and platinum sheet serving as the anode and cathode, respectively. The electrolyte was composed of 0.5 wt % ammonium fluoride (NH_4F) in ethylene glycol (EG) with 2 vol % deionized water. During the process, the titanium plate and platinum sheet were immersed in the prepared electrolyte, and anodization was carried out at 60 V for 40 min, leading to the growth of a TiO_2 layer on the surface of the titanium plate. Following anodization, the samples were rinsed with deionized water and dried at room temperature. The dried specimens were then heated in a muffle furnace at 500 °C in air with a ramp rate of 2 °C/min and held for 2 h to yield the TiO_2/TP. Powder samples were subsequently scraped from the titanium plates for further processing.

2.4. Synthesis of TiO_{2-x}/TP. The prepared TiO_2/TP was placed in a quartz tube, which was initially evacuated by using a vacuum pump and then filled with hydrogen gas. The sample was subsequently heated to 500 °C at a rate of 5 °C/min and maintained at this temperature for 4 h in a H_2 atmosphere-5% H_2 (Ar). Afterward, it was cooled to room temperature under a continuous flow of hydrogen gas. This process resulted in the formation of an oxygen vacancy-enriched TiO_{2-x}/TP electrode. Powder samples were scraped from the titanium plates for further processing.

2.5. Synthesis of TiO_{2-x}(TiO_2)/FTO. TiO_2 and TiO_{2-x} photoanodes were prepared by using the drop-casting technique. Fluorine-doped tin oxide (FTO) conducting glass substrates (2 × 2 cm^2) were cleaned sequentially by sonication in acetone, ethanol, and deionized water for 15 min each and then dried using nitrogen purging. A total of 20 mg of TiO_2 (or TiO_{2-x}, calcined at 500 °C for 4 h under a hydrogen atmosphere) powder was dispersed in a solution containing 1 mL of water and 1 mL of ethanol. The mixture was sonicated for 2 h in a cold-water bath. Subsequently, 0.5 mL of the prepared dispersion was uniformly applied to the FTO glass (effective area of 2 cm^2) and dried at 100 °C for 30 min to enhance adhesion.

2.6. Ozone Removal Experiment. Ozone removal of ozone was achieved by passing ozone gas into the KI/KOH electrolyte. In this case, the volume of the electrolyte was 50 mL, and the composition was 0.2 M KI and 1 M KOH.

Electrochemical catalysis for ozone removal: the ozone gas flow rate was 300 mL/min, and the ozone concentration was 500 ppm. The electrodes used were TiO_{2-x}/TP electrodes for the cathode and Pt sheet electrodes for the anode. The actual running area of the cathode electrode was 1 cm^2, and the current was 0.2 A. In the high-concentration ozone removal experiment, the ozone concentration was increased to 1500 ppm, and the rest of the experimental conditions were not changed.

Photoelectrochemical catalysis for ozone removal: the ozone gas flow rate was 300 mL/min, and the ozone concentration was 50 ppm. The electrodes used were TiO_{2-x}/FTO electrodes for the cathode and Pt sheet electrodes for the anode. The actual running area of the

https://doi.org/10.1021/cbe.4c00187
Chem Bio Eng. 2025, 2, 322−331

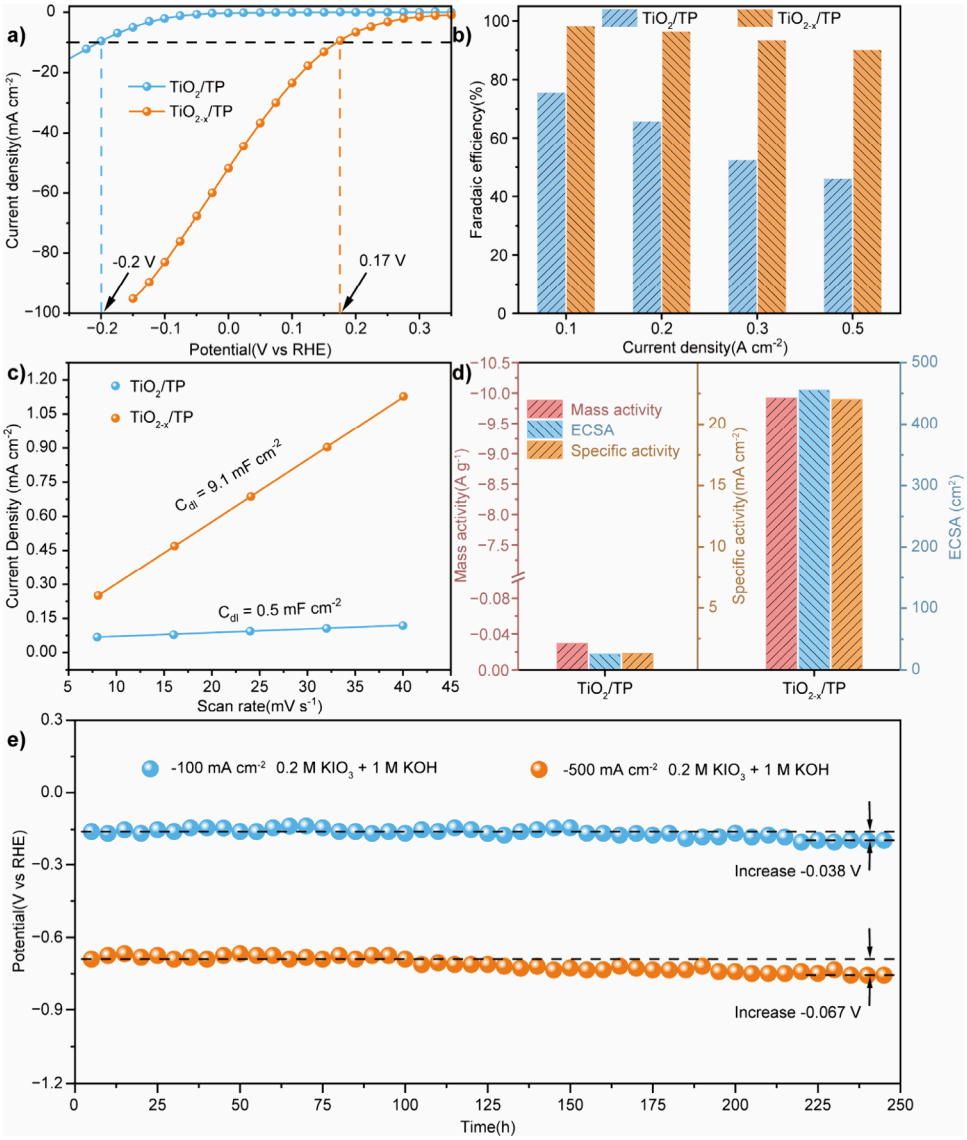

Figure 3. (a) LSV curves of TiO_{2-x}/TP electrode and TiO_2/TP electrode. (b) Faradaic efficiency of TiO_{2-x}/TP electrodes and TiO_2/TP electrodes at different current densities. (c) C_{dl} values obtained from CV curves for TiO_{2-x}/TP electrodes and TiO_2/TP electrodes. (d) MA, ECSA, and SA values for TiO_{2-x}/TP and TiO_2/TP electrodes. (e) TiO_{2-x}/TP electrode stability test curve (TiO_{2-x} calcination conditions: 500 °C for 4 h under a H_2 atmosphere).

cathode electrode was 2 cm^2, and the current was 0.02 A. A 500 W Xe lamp (Perfect Light FX 3000, equipped with an AM 1.5 G filter) was employed to simulate 1 sun illumination. The light intensity was calibrated to 100 $mW{\cdot}cm^{-2}$ by a standard irradiatometer.

Ozone was generated by an ozone generator (CH-ZTW6G, CHUAVG, China) and detected by an ozone detector (Model 106-M, 2B Technologies, USA).

3. RESULTS AND DISCUSSION

3.1. Characterization of Electrode Morphology and Composition. The synthesis process of the TiO_{2-x}/TP cathode is shown in Figure 1a, which includes anodic oxidation as well as a hydrogen calcination step. The pretreatment of the Ti plate makes the surface rough (Figure 1b). The AFM test data in Figure S1 prove this result. Immediately after anodization as well as calcination treatment, a layer of in situ grown porous TiO_2 was obtained on the surface of the TP (Figure 1c). Finally, it was calcined under a hydrogen atmosphere, and TiO_{2-x}/TP was obtained by the reduction of hydrogen (Figures S2 and S3). The results of the BET tests in Figure S4 and Table S1 show that the specific surface area, pore size, and pore volume of TiO_{2-x} samples were partially increased after the hydrogen calcination treatment. The results of XRD (Figure 1d) show that TiO_2 and TiO_{2-x} are highly crystalline, and both are TiO_2 with a single anatase phase. In the high-resolution transmission electron microscopy (HRTEM) images (Figure 1e), TiO_{2-x} has many visible lattice defects, which is strong evidence of the successful introduction of oxygen vacancies.

3.2. Characterization of Oxygen Vacancy Defects at Electrodes. To show more clearly the difference in oxygen vacancy concentration between TiO_2 and TiO_{2-x} samples, they were characterized by XPS, Raman spectroscopy, and EPR as shown below.

In the Ti 2p spectra (Figure 2a and Figure S5), the peaks near 459 and 465 eV belong to Ti^{4+} $2p_{3/2}$ and Ti^{4+} $2p_{1/2}$, respectively.[27,28] It can be seen that the binding energies of both peaks of the TiO_{2-x} sample are lower than those of the

https://doi.org/10.1021/cbe.4c00187
Chem Bio Eng. 2025, 2, 322−331

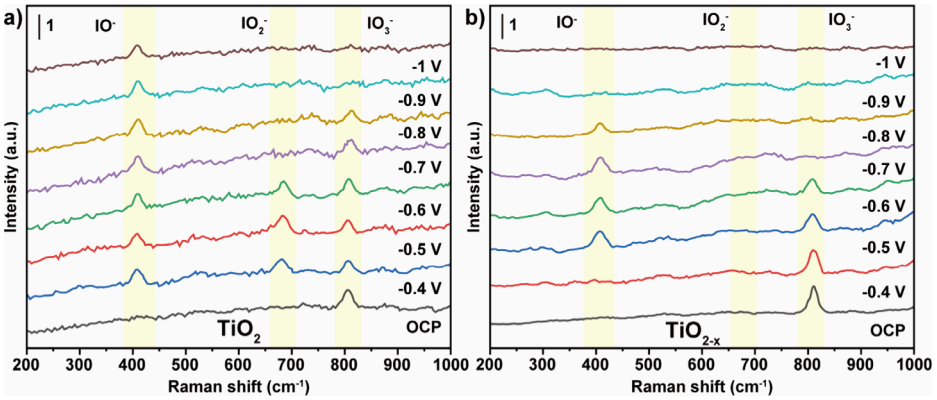

Figure 4. SHINERS spectra of (a) TiO_2 and (b) TiO_{2-x} samples at different potentials (TiO_{2-x} calcination conditions: 500 °C for 4 h under a H_2 atmosphere).

TiO_2 sample. In the O 1s spectra (Figure 2b and Figure S5), three peaks can be classified near 530, 531.5, and 532.5 eV, which correspond to surface lattice oxygen (O_L), surface oxygen vacancies (O_V), and chemisorbed oxygen (O_c), respectively. It can be seen that the surface oxygen vacancy peak area of TiO_{2-x} samples synthesized under different conditions are enhanced compared to that of the TiO_2 sample.[29,30]

As shown in the Raman spectra (Figure 2c), both TiO_2 and TiO_{2-x} samples have obvious signals near 150, 200, 390, 500, and 620 cm^{-1}, which are consistent with the standard peak signals of the TiO_2 anatase phase.[31] However, as can be seen in the 110−190 cm^{-1} localized magnification, the peak position of the TiO_{2-x} sample is shifted to the right compared to that of the TiO_2 sample, which is attributed to the phonon confinement due to the oxygen vacancies.[32]

In the EPR spectra (Figure 2d and Figure S6), the intensity of the peak at g = 2.003 is proportional to the oxygen vacancy concentration of the sample. From Figure 2d and Figure S6, it can be seen that the peak intensity at g = 2.003 of the TiO_{2-x} sample is significantly stronger than that of the TiO_2 sample.[4,33,34]

The above series of characterization results all show that the oxygen vacancy concentration of TiO_{2-x} samples obtained after the high-temperature calcination treatment of TiO_2 samples with hydrogen is significantly enhanced. Among them, the TiO_{2-x} samples obtained by calcination at 500 °C for 4 h in a H_2 atmosphere have the highest oxygen vacancy concentration.

3.3. Electrochemical Performance Testing. In order to evaluate the electrochemical performance of the TiO_{2-x}/TP cathode for IO_3RR, the electrode was tested through a standard three-electrode system in a 0.2 M KIO_3 + 1 M KOH solution. First, the samples with different calcination temperatures and times were analyzed by linear scanning voltammetry (LSV) and electrochemical impedance spectroscopy (EIS). The LSV curves responded to the catalytic performance of the electrode, while the EIS responded to the electrochemical impedance of the electrode.[35−37] It can be seen that the sample obtained by calcining at 500 °C for 4 h has the best IO_3RR performance and the fastest electron transport rate (Figure S7). Combined with the previous data, 500 °C calcination for 4 h was identified as the synthesis conditions for TiO_{2-x}/TP electrodes.

The LSV curves in Figure 3a show that the TiO_{2-x}/TP cathode only requires 0.17 V to reach a current density of 10 mA/cm^2, which is much higher than the −0.20 V of the TiO_2/TP electrode. In addition, the Tafel slope plots obtained from the LSV curves as well as the EIS curves of the electrodes also clearly reflect the high IO_3RR kinetics as well as the low interfacial resistance of the TiO_{2-x}/TP electrodes (Figure S8).

In the electrochemical reduction of IO_3^-, the reactions occurring at the cathode and anode are shown in Figure S9. The hydrogen evolution reaction (HER) at the cathode is a side reaction. The Faradaic efficiency of the electrodes is an important metric for evaluating the electrodes.[38] As can be seen from Figure 3b, the Faradaic efficiency of the TiO_{2-x}/TP electrode for IO_3RR at different current densities is 95% on average (Figure S10). At a high current density of 0.5 A/cm^2, the Faradaic efficiency of the TiO_{2-x}/TP electrode is also close to 90%, which is much higher than that of the TiO_2/TP electrode (46%). Furthermore, the TiO_{2-x}/TP cathode also offers significant advantages over other common cathode materials, combining both low overpotential and high Faradaic efficiency (Figure S11).

Based on the cyclic voltammetry (CV) curves (Figure S12) of the samples at different sweep speeds, the corresponding double-layer capacitance (C_{dl}) values can be calculated.[39−42] Figure 3c shows that the C_{dl} of the TiO_{2-x}/TP electrode (9.1 mF/cm^2) is significantly higher than that of the TiO_2/TP electrode (0.5 mF/cm^2). The electrochemically active surface area (ECSA) of the electrode was estimated by comparing the C_{dl} value of the electrode with the C_s value (60 $\mu F/cm^2$) of the ideal smooth oxide bilayer capacitance. The specific activity (SA) could be further obtained by combining with the current at 0.17 V vs RHE (Figure 3d). The values of ECSA (455 cm^2) as well as SA (21.98 mA/cm^2) of the TiO_{2-x}/TP electrode were significantly improved compared to those of the TiO_2/TP electrode. Using the LSV curve of the electrode and the catalyst mass, the catalyst mass activity (MA) at different potentials can be obtained (Figure 3d). The TiO_{2-x}/TP electrode exhibited a mass activity of −10 A/g, which was much higher than that of the TiO_2/TP electrode (−0.03 A/g) at 0.17 V vs RHE.

Stability is an important indicator of whether the electrode is of practical value. In this paper, the stability of TiO_{2-x}/TP electrodes was evaluated using the constant current timing method at both 100 and 500 mA/cm^2. The results in Figure 3e show that the stability of the TiO_{2-x}/TP electrode is greater than 250 h under the two current density conditions. The SEM and XRD results (Figure S13) after the stability test also reflect

https://doi.org/10.1021/cbe.4c00187
Chem Bio Eng. 2025, 2, 322−331

that there is no obvious damage to the composition and morphology of the electrodes.

3.4. Analysis of the IO_3^- Electrochemical Reduction Process. In order to further understand the reduction of IO_3^- at the TiO_{2-x}/TP electrode, the process was analyzed using shell-isolated nanoparticle-enhanced Raman spectroscopy (SHINERS).[43−45] The SHINERS technique uses Au@SiO_2 colloidal dispersions as signal enhancers and can detect extremely weak Raman signal changes. In SHINERS, the Raman peaks near 800, 685, and 430 cm^{-1} are attributed to IO_3^-, IO_2^-, and IO^-, respectively,[46] which suggests that the reduction process of IO_3^- at the cathode, as shown below, is a one-by-one detachment of O atoms.

$$IO_3^- + 2e^- + H_2O \rightarrow IO_2^- + 2OH^- \quad (3\text{-}1)$$

$$IO_2^- + 2e^- + H_2O \rightarrow IO^- + 2OH^- \quad (3\text{-}2)$$

$$IO^- + 2e^- + H_2O \rightarrow I^- + 2OH^- \quad (3\text{-}3)$$

In SHINERS measurement, different potentials (−0.4 to −1 V) were used for TiO_2 as well as TiO_{2-x} samples, respectively, to detect the Raman signal changes during the electrochemical reduction process of IO_3^- (Figure 4). First, Raman peaks belonging to IO_3^- were detected on both TiO_2 and TiO_{2-x} samples when no voltage was applied, but the peak intensity was higher on TiO_{2-x} samples compared to that on TiO_2 samples, which suggests that the adsorption of IO_3^- on TiO_{2-x} was stronger. With the gradual increase in voltage, the Raman peaks belonging to IO_3^- on the TiO_{2-x} samples were not detected at −0.7 V, while the Raman peaks belonging to IO_3^- on the TiO_2 samples were not detected at −0.9 V. The Raman peak strengths belonging to IO_3^- are related to the adsorption and reaction rates. The adsorption rate is usually considered to be constant, while the reaction rate increases with increasing voltage. The lower vanishing voltages of the IO_3^- Raman peaks on the TiO_{2-x} samples further reflect its superior IO_3RR performance over TiO_2.

As the test voltage continued to change, the Raman peaks of IO_2^- as well as IO^- were detected. Among them, the Raman peaks belonging to IO_2^- disappeared at lower voltages, and its peaks were not even detected on the TiO_{2-x} samples. However, Raman peaks belonging to IO^- were detected on both TiO_2 and TiO_{2-x} samples, and their vanishing voltages were higher than those of the IO_3^- Raman peaks, which reflects that the reduction of IO^- to I^- in IO_3RR is the slowest among the three steps and is the decisive step of the reaction.

3.5. DFT Calculation. In order to gain a more in-depth understanding of the phenomena in the experiments, density functional theory (DFT) was used for theoretical calculation of the samples.[19,47−49]

First, as shown in Figure S14, TiO_2 as well as TiO_{2-x} samples were constructed. Their density of states (DOS) plots reflect that the introduction of oxygen vacancies in TiO_2 causes the overall energy band of the sample to move down to below the Fermi energy level, and electrons are more likely to jump to the Fermi energy level, enhancing the conductivity of the sample.

The hydrogen evolution reaction (HER) acts as a competing reaction to IO_3RR, as shown in Figure 5a, and the introduction of oxygen vacancies on the TiO_2 samples inhibits the adsorption of H atoms on the samples, which in turn inhibits the occurrence of HER. In addition, the adsorption energy of IO_3^- on the TiO_{2-x} sample is also larger than that on the TiO_2 sample, as shown in Figure 5b. All of these data indicate that the TiO_{2-x} sample has higher selectivity for IO_3RR compared to HER.

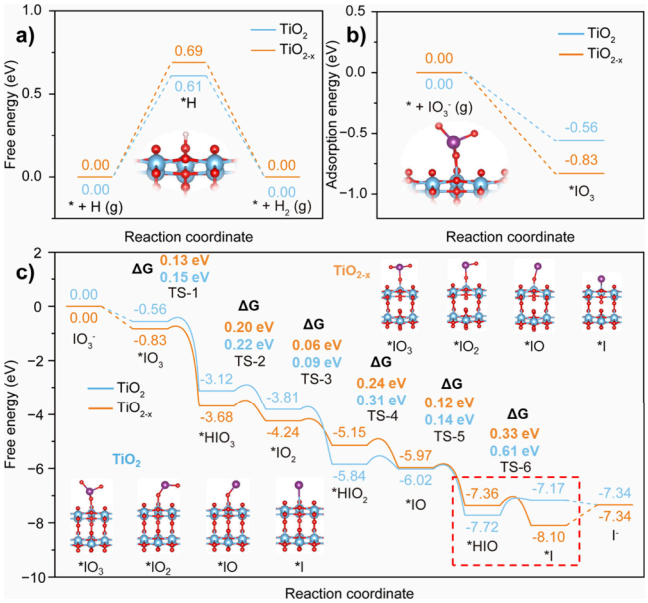

Figure 5. (a) Calculated free energy changes of HER on TiO_2 (101) and TiO_{2-x} (101) surfaces. (b) Calculated adsorption energies of IO_3^- on TiO_2 and TiO_{2-x} surfaces. (c) Calculated free energy changes of IO_3RR on TiO_2 (101) and TiO_{2-x} (101) surfaces (transition state abbreviated as TS).

Finally, the IO_3RR process was calculated by using TiO_2 and TiO_{2-x} samples. As shown in Figure 5c, the introduction of oxygen vacancies in the IO_3RR process greatly reduces the energy barrier for the reduction of the *HIO to *H reaction and optimizes the IO_3RR process, which is consistent with the SHINERS results discussed above. In addition, it can be seen that the activation energy required for each step of the reaction in the IO_3RR process of the TiO_{2-x} sample is smaller than that of the TiO_2 sample, which greatly proves that the TiO_{2-x} sample has superior IO_3RR kinetics.

3.6. TiO_{2-x}/TP Cathode Applied to I^-/IO_3^- System for Ozone Removal Experiments. The results described above indicate that the TiO_{2-x}/TP cathode has abundant active sites and exhibit excellent IO_3RR performance. In order to verify the potential application of the TiO_{2-x}/TP electrode, it was applied to the I^-/IO_3^- system for a long-term ozone removal experiment. As seen in the experimental procedure and setup shown in Figure S15 and Figure 6a, ozone gas was passed into the KI/KOH electrolyte, and the ozone concentration was measured at the outlet to determine the ozone removal effect. The electrolysis was cycled by using TiO_{2-x}/TP electrodes as cathodes and Pt sheet electrodes as anodes. As shown in Figure 6b, the system was able to maintain 100% ozone conversion after 30 days, reflecting the ability of the method to remove ozone continuously and efficiently over a long period of time. In addition, the system has been applied to the removal of high concentrations of ozone (1500 and 2000 ppm). As shown in Figure S16, the system was able to maintain a stable removal rate for high concentrations of ozone at the beginning of the process, but after a period of operation, the ozone conversion rate decreased. This is related to the electron supply of the system current and the stability of the electrodes. SEM and XRD tests on the tested electrodes (Figure S17) showed that

https://doi.org/10.1021/cbe.4c00187
Chem Bio Eng. 2025, 2, 322−331

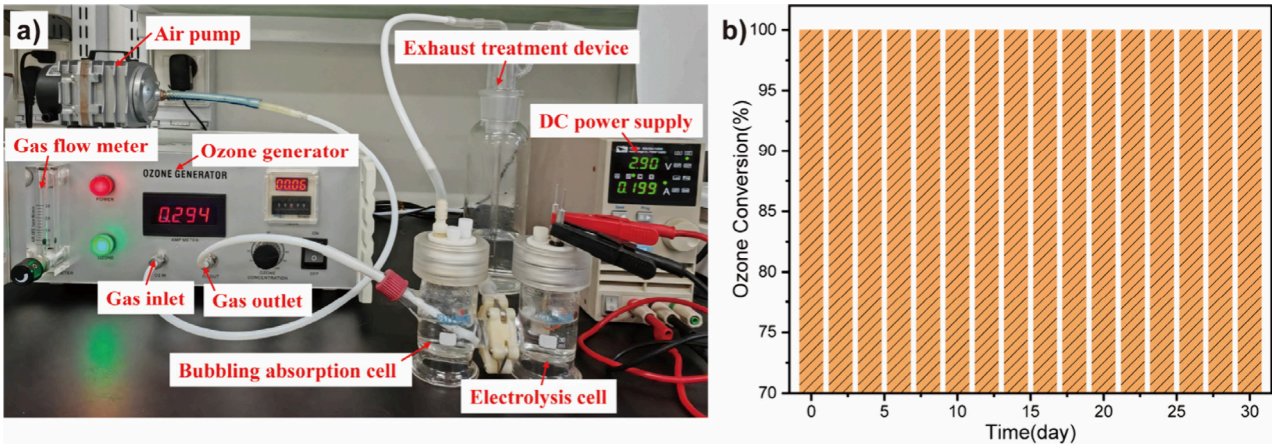

Figure 6. (a) Ozone removal device diagram. (b) Ozone removal by TiO_{2-x}/TP electrode applied to I^-/IO_3^- system (ozone gas flow rate: 300 mL/min; ozone concentration: 500 ppm; TiO_{2-x} calcination conditions: 500 °C for 4 h under a H_2 atmosphere).

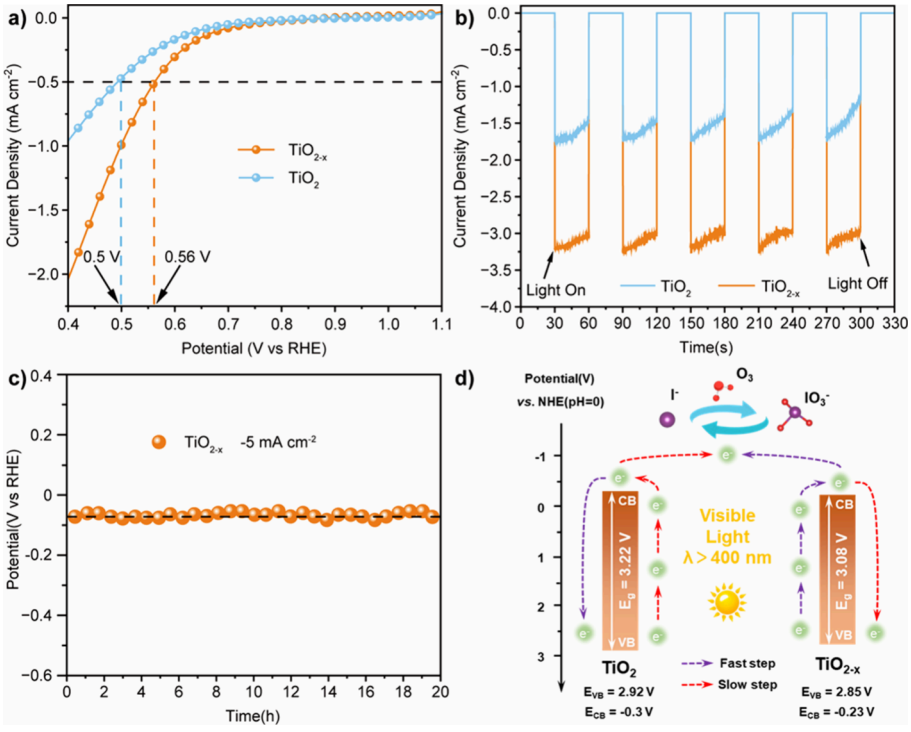

Figure 7. (a) LSV curves and (b) transient photocurrent response spectra of different photoanodes. (c) Photocurrent stability test of TiO_{2-x}/FTO. (d) Schematic of TiO_2 and TiO_{2-x} photoelectrochemical reduction of IO_3^- (TiO_{2-x} calcination conditions: 500 °C for 4 h under a H_2 atmosphere).

the composition of the electrodes did not change, and the dissolution precipitation (Figure S18) on the surface of the electrode material leading to the destruction of the electrode structure might be the reason for the degradation of the system performance.

In terms of operating costs, as shown in Section S2 (Economic Analysis) of the Supporting Information, applying TiO_{2-x}/TP electrodes to the I^-/IO_3^- system removes 1 kg of ozone for only $3.72, which is on average one-third of the ozone treatment cost of recently reported ozone decomposition catalysts, one-fifth of the ozone treatment cost of activated carbon adsorption, and 1/83 333 of the ozone treatment cost of thermal decomposition. These data reflect the great economic benefits of the method.

3.7. Photoelectrochemical Performance Testing. In addition to its excellent electrocatalytic properties, TiO_2 also excels in photocatalysis. The photoelectrochemical reduction method would be a better method for IO_3^- reduction than electrocatalysis alone. In order to verify the photoelectrochemical performance of TiO_{2-x} materials, a series of characterizations and testing were carried out.

The incident photocurrent conversion efficiency (IPCE) spectra show an IPCE value of 55% for TiO_{2-x} after hydrogen calcination treatment (Figure S19).[21] For this sample, a band gap of $E_g \approx 3.08$ eV can be determined (Figure S20). Compared to the initial TiO_2 sample with an IPCE of 39% and an E_g of ~3.22 eV, there is a significant improvement. Also, the intensity of the TiO_{2-x} sample is significantly weaker than that of the TiO_2 sample in the photoluminescence (PL) emission

https://doi.org/10.1021/cbe.4c00187
Chem Bio Eng. 2025, 2, 322−331

spectrum (Figure S21). These data indicate that the recombination of electron−hole pairs is also suppressed in the TiO_{2-x} sample after hydrogen treatment with a smaller band gap, suggesting that it is an excellent photocatalytic material. In addition, as seen in the UV−visible spectra shown in Figure S22, the absorption intensity of TiO_{2-x} samples in the UV region is reduced compared to that of TiO_2, but the absorption in the visible region is significantly increased. Overall, the TiO_{2-x} samples showed better absorption of light at wavelengths from 200 to 800 nm.

In this paper, TiO_2 and TiO_{2-x} loaded on fluorine-doped tin oxide (FTO) conducting glass substrates were prepared as photocathodes using the drop-casting method (Figure S23). The LSV curves in Figure 7a show that the TiO_{2-x}/FTO photocathode provides a significantly higher photocurrent than TiO_2/FTO. Figure S24 demonstrates the corresponding energy conversion curves, with a half-cell solar-to-iodide (HC-STI) conversion efficiency of 0.28% for the TiO_{2-x}/FTO photocathode, which is higher than that for the TiO_2/FTO photocathode (0.13%). In addition, we performed transient photocurrent and photoelectrochemical impedance spectroscopy (EIS) measurements. The photocurrent transient (Figure 7b) shows the remarkable photocurrent response of the TiO_{2-x}/FTO photocathode material, and the EIS results (Figure S25) show that the charge transfer resistance of TiO_{2-x}/FTO is significantly lower than that of TiO_2/FTO. These results demonstrate the excellent photoelectrochemical performance of TiO_{2-x}. In addition, the potential of TiO_{2-x}/FTO was not significantly degraded after 20 h of continuous illumination under certain current density conditions (Figure 7c). The XRD and SEM (Figure S26) results after the stability tests also showed no significant changes in the electrode structure and composition.

Finally, a schematic of TiO_2 and TiO_{2-x} photoelectrochemical reduction of IO_3^- is presented. In the photoelectrochemical reaction, as shown in Figure 7d, TiO_{2-x} has a narrower band gap and electron−hole pairs that are less prone to recombination, which results in a stronger photovoltaic response and thus a more excellent IO_3RR performance. The excellent photoelectrochemical properties of TiO_{2-x} provide a cleaner and more efficient method for ozone removal by I^-/IO_3^- systems, demonstrating the possibility of solar energy as a recycled energy source for I^-/IO_3^- systems.

Combining the above experimental and theoretical calculations, we can know that the introduction of oxygen vacancies makes TiO_{2-x} have excellent electrical conductivity as well as very high selectivity to IO_3^- and at the same time reduces the band gap of TiO_{2-x}, as well as inhibits the recombination of its electron−hole pairs, which results in an excellent photoelectrochemical reduction performance. In addition, the stable structure and composition of TiO_{2-x}/TP and TiO_{2-x}/FTO allow the whole system to exhibit excellent stability. All of these results indicate that the TiO_{2-x} electrode with a high oxygen vacancy concentration has excellent suitability for the I^-/IO_3^- cycling system.

As shown in Figure S27, stability experiments for ozone removal by the I^-/IO_3^- photoelectrochemical system were performed. Under the test conditions (ozone concentration: 50 ppm; gas flow rate: 300 mL/min), the system showed excellent durability: after 10 days of continuous operation, the ozone conversion rate only decreased by about 5%. It is noteworthy that this performance decay occurred mainly during the last 5 days, while the ozone removal rate remained relatively stable during the first 5 days.

4. CONCLUSION

In this paper, we employed a combination of photoelectrochemical reduction and solution absorption methods to achieve the efficient and continuous removal of ozone gas. The introduction of oxygen vacancies on the TiO_{2-x} electrode enhanced the IO_3^- adsorption effect and lowered the energy barrier for the IO_3RR process, resulting in excellent IO_3RR performance. We applied the TiO_{2-x}/TP electrode to the I^-/IO_3^- system for long-term ozone removal, which demonstrated stable operational capability with a 100% ozone removal rate after 30 days. Furthermore, the exceptional photoelectrochemical performance exhibited by TiO_{2-x}/FTO enables the realization of a solar-driven I^-/IO_3^- photoelectrochemical cycling system. The outstanding efficacy in ozone removal, coupled with low operating expenses and environmentally friendly processes, unequivocally demonstrates the applicability of this method for industrial application.

■ ASSOCIATED CONTENT

Supporting Information

The Supporting Information is available free of charge at https://pubs.acs.org/doi/10.1021/cbe.4c00187.

Description of electrochemical and photoelectrochemical measurements, characterization methods, I^- concentration measurements, economic analysis of different ozone treatment methods, and density functional theory (DFT) calculations; calculation of relevant parameters; and other supporting figures and tables with additional characterization data (PDF)

■ AUTHOR INFORMATION

Corresponding Authors

Xingwang Zhang − *Key Laboratory of Biomass Chemical Engineering of Ministry of Education, Department of Chemical and Biological Engineering, Zhejiang University, Hangzhou 310027, China;* orcid.org/0000-0002-8564-4678; Email: xwzhang@zju.edu.cn

Chunlin Yu − *Key Laboratory of Biomass Chemical Engineering of Ministry of Education, Department of Chemical and Biological Engineering, Zhejiang University, Hangzhou 310027, China; Institute of Zhejiang University-Quzhou, Quzhou 324000, China*; Email: chunlinyu@zju.edu.cn

Authors

Jiahong Liao − *Key Laboratory of Biomass Chemical Engineering of Ministry of Education, Department of Chemical and Biological Engineering, Zhejiang University, Hangzhou 310027, China*

Wenyi Wang − *Key Laboratory of Biomass Chemical Engineering of Ministry of Education, Department of Chemical and Biological Engineering, Zhejiang University, Hangzhou 310027, China; Institute of Zhejiang University-Quzhou, Quzhou 324000, China*

Weicheng Tong − *Zhejiang Quzhou Jusu Chemical Co., Ltd., Quzhou 324004, China*

Lixia Qiu − *Zhejiang Quzhou Jusu Chemical Co., Ltd., Quzhou 324004, China*

Hao Cheng − *Zhejiang Quzhou Jusu Chemical Co., Ltd., Quzhou 324004, China*
Xinben Zhao − *Zhejiang Quzhou Jusu Chemical Co., Ltd., Quzhou 324004, China*
Yi He − *Key Laboratory of Biomass Chemical Engineering of Ministry of Education, Department of Chemical and Biological Engineering, Zhejiang University, Hangzhou 310027, China; Institute of Zhejiang University-Quzhou, Quzhou 324000, China;* orcid.org/0000-0002-8807-0892

Complete contact information is available at: https://pubs.acs.org/10.1021/cbe.4c00187

Notes

The authors declare no competing financial interest.

■ ACKNOWLEDGMENTS

This study was financially supported by the Science and Technology Plan Project of Quzhou (2023K008), the National Natural Science Foundation of China (22238008), the Research Funds of the Institute of Zhejiang University-Quzhou (IZQ2021RCZX038, IZQ2022RCZX01, IZQ2022RCZX017), and the Central University Basic Research Fund of China (No. 226-2022-00055).

■ REFERENCES

(1) Ma, J.; Wang, C.; He, H. Transition Metal Doped Cryptomelane-type Manganese Oxide Catalysts for Ozone Decomposition. *Appl. Catal., B* **2017**, *201*, 503−510.
(2) Zhu, G.; Zhu, J.; Li, W.; Yao, W.; Zong, R.; Zhu, Y.; Zhang, Q. Tuning the K^+ Concentration in the Tunnels of α-MnO_2 To Increase the Content of Oxygen Vacancy for Ozone Elimination. *Environ. Sci. Technol.* **2018**, *52* (15), 8684−8692.
(3) Ma, J.; Li, X.; Zhang, C.; Ma, Q.; He, H. Novel $CeMn_aO_x$ Catalyst for Highly Efficient Catalytic Decomposition of Ozone. *Appl. Catal., B* **2020**, *264*, 118498.
(4) Wu, Z.; Zhang, P.; Rong, S.; Jia, J. Creating Water-resistant Oxygen Vacancies in δ-MnO_2 by Chlorine Introduction for Catalytic Ozone Decomposition at Ambient Temperature. *Appl. Catal., B* **2023**, *335*, 122900.
(5) Ma, J.; Chen, Y.; He, G.; He, H. A Robust H-transfer Redox Mechanism Determines the High-efficiency Catalytic Performance of Layered Double Hydroxides. *Appl. Catal., B* **2021**, *285*, 119806.
(6) Hellén, H.; Kuronen, P.; Hakola, H. Heated Stainless Steel Tube for Ozone Removal in the Ambient Air Measurements of Mono- and Sesquiterpenes. *Atmos. Environ.* **2012**, *57*, 35−40.
(7) Beltrán, F. J.; Rivas, J.; Álvarez, P.; Montero-de-Espinosa, R. Kinetics of Heterogeneous Catalytic Ozone Decomposition in Water on an Activated Carbon. *Ozone-Sci. Eng.* **2002**, *24* (4), 227−237.
(8) Wang, Z.; Li, X.; Ma, J.; He, H. Effect of Interlayer Anions on NiFe Layered Double Hydroxides for Catalytic Ozone Decomposition. *Environ. Sci. Technol.* **2024**, *58* (19), 8597−8606.
(9) Wang, Z.; Li, T.; Zhang, S.; Zhang, R.; Zhang, Y.; Zhong, Q. One-step Synthesis of δ-MnO_2 with Rich Defects for Efficient Ozone Decomposition under Humid Conditions. *Chem. Eng. J.* **2024**, *488*, 150693.
(10) Ryu, S.-H.; Kim, G.; Gupta, S.; Bhattacharjee, S.; Lee, S.-C.; Lee, H.; Choi, J.-H.; Jeong, H. Improved Resistance to Water Poisoning of Pd/CeO_2 Monolithic Catalysts by Heat Treatment for Ozone Decomposition. *Chem. Eng. J.* **2024**, *485*, 149487.
(11) Liu, B.; Yi, Z.; Yang, Y.; Li, Y.; Yang, J.; Zhu, M. Unlocking Efficient and Robust Ozone Decomposition with CNT-confined Manganese Oxide via Synergistic Electronic Modulation. *Appl. Catal., B* **2023**, *334*, 122788.
(12) Helmig, D. Ozone Removal Techniques in the Sampling of Atmospheric Volatile Organic Trace Gases. *Atmos. Environ.* **1997**, *31*, 3635−3651.
(13) Williams, E. L.; Grosjean, D. Removal of Atmospheric Oxidants with Annular Denuders. *Environ. Sci. Technol.* **1990**, *24*, 811−814.
(14) Liao, J.; Cheng, H.; Fang, Y.; Zhang, Y.; Zhao, X.; Qiu, L.; Cai, X.; Zhang, X. Regeneration of Ozone Decomposition Catalysts by Elimination of O_2^{2-} from Oxygen Vacancies. *J. Environ. Chem. Eng.* **2024**, *12* (5), 113573.
(15) Li, H.; Zhang, P.; Jia, J.; Wang, X.; Rong, S. A Cobalt-vacant Co_3O_4 as a Stable Catalyst for Room-temperature Decomposition of Ozone in Humid Air. *Appl. Catal., B* **2024**, *340*, 123222.
(16) Cros, C. J.; Morrison, G. C.; Siegel, J. A.; Corsi, R. L. Long-term Performance of Passive Materials for Removal of Ozone from Indoor Air. *Indoor Air* **2012**, *22* (1), 43−53.
(17) Chen, R.; Shen, S.; Wang, K.; Wang, J.; Yang, W.; Li, X.; Li, J.; Dong, F. Promoting the Efficiency and Selectivity of NO_3^--to-NH_3 Reduction on Cu-O-Ti Active Sites via Preferential Glycol Oxidation with Holes. *Proc. Nat. Acad. Sci. U.S.A.* **2023**, *120*, e2312550120.
(18) Zhang, S.; Wu, J.; Zheng, M.; Jin, X.; Shen, Z.; Li, Z.; Wang, Y.; Wang, Q.; Wang, X.; Wei, H.; Zhang, J.; Wang, P.; Zhang, S.; Yu, L.; Dong, L.; Zhu, Q.; Zhang, H.; Lu, J. Fe/Cu Diatomic Catalysts for Electrochemical Nitrate Reduction to Ammonia. *Nat. Commun.* **2023**, *14* (1), 3634.
(19) Zhang, R.; Li, C.; Cui, H.; Wang, Y.; Zhang, S.; Li, P.; Hou, Y.; Guo, Y.; Liang, G.; Huang, Z.; Peng, C.; Zhi, C. Electrochemical Nitrate Reduction in Acid Enables High-efficiency Ammonia Synthesis and High-voltage Pollutes-based Fuel Cells. *Nat. Commun.* **2023**, *14* (1), 8036.
(20) Murphy, E.; Liu, Y.; Matanovic, I.; Rüscher, M.; Huang, Y.; Ly, A.; Guo, S.; Zang, W.; Yan, X.; Martini, A.; Timoshenko, A.; Cuenya, B.; Zenyuk, I.; Pan, X.; Spoerke, E.; Atanassov, P. Elucidating Electrochemical Nitrate and Nitrite Reduction over Atomically-dispersed Transition Metal Sites. *Nat. Commun.* **2023**, *14* (1), 4554.
(21) Wu, S.-M.; Wu, L.; Denisov, N.; Badura, Z.; Zoppellaro, G.; Yang, X.-Y.; Schmuki, P. Pt Single Atoms on TiO_2 Can Catalyze Water Oxidation in Photoelectrochemical Experiments. *J. Am. Chem. Soc.* **2024**, *146* (24), 16363−16368.
(22) Jia, R.; Wang, Y.; Wang, C.; Ling, Y.; Yu, Y.; Zhang, B. Boosting Selective Nitrate Electroreduction to Ammonium by Constructing Oxygen Vacancies in TiO_2. *ACS Catal.* **2020**, *10* (6), 3533−3540.
(23) Li, Z.; Zhou, Q.; Liang, J.; Zhang, L.; Fan, X.; Zhao, D.; Cai, Z.; Li, J.; Zheng, D.; He, X.; Luo, Y.; Wang, Y.; Ying, B.; Yan, H.; Sun, S.; Zhang, J.; Alshehri, A.; Gong, F.; Zheng, Y.; Sun, X. Defective TiO_{2-x} for High Performance Electrocatalytic NO Reduction toward Ambient NH_3 Production. *Small* **2023**, *19* (24), 2300291.
(24) Gao, J.; Xue, J.; Jia, S.; Shen, Q.; Zhang, X.; Jia, H.; Liu, X.; Li, Q.; Wu, Y. Self-Doping Surface Oxygen Vacancy-Induced Lattice Strains for Enhancing Visible Light-Driven Photocatalytic H_2 Evolution over Black TiO_2. *ACS Appl. Mater. Interfaces* **2021**, *13* (16), 18758−18771.
(25) Naldoni, A.; Altomare, M.; Zoppellaro, G.; Liu, N.; Kment, Š.; Zbořil, R.; Schmuki, P. Photocatalysis with Reduced TiO_2: From Black TiO_2 to Cocatalyst-Free Hydrogen Production. *ACS Catal.* **2019**, *9* (1), 345−364.
(26) Xu, L.; Jiang, Q.; Xiao, Z.; Li, X.; Huo, J.; Wang, S.; Dai, L. Plasma Engraved Co_3O_4 Nanosheets with Oxygen Vacancies and High Surface Area for the Oxygen Evolution Reaction. *Angew. Chem., Int. Ed.* **2016**, *55* (17), 5277−5281.
(27) Tian, X.; Han, W.; Zeng, Z.; He, Y.; Lei, L.; Xu, X.; Xu, X.; Xu, Y.; Li, P.; Zhang, X. Oleyl Phosphate-Modified Crystalline-Amorphous TiO_2/Ce_2O_3 Heterojunction nanoparticles with Significantly Reduced Photocatalytic Activity as Stable UV-Shielding fillers. *Chem. Eng. J.* **2023**, *477*, 146962.
(28) Zhang, Y.; Zhang, X.; Yang, P.; Gao, M.; Feng, J.; Li, D. In situ Topologically Induced PtZn Alloy @ $ZnTiO_x$ and the Synergistic Effect on Glycerol Oxidation. *Appl. Catal., B* **2021**, *298*, 120634.
(29) Zhang, L.; Yang, J.; Wang, A.; Chai, S.; Guan, J.; Nie, L.; Fan, G.; Han, N.; Chen, Y. High Performance Ozone Decomposition

Spinel $(Mn,Co)_3O_4$ Catalyst Accelerating the Rate-determining Step. *Appl. Catal., B* **2022**, *303*, 120927.
(30) Shi, Y.; Qiu, J.; Xue, Y.; Ding, X.; Dai, J.; Sun, X.; Zhao, M.; Wang, J.; Chen, Y. Catalysts for Highly Water-resistant Catalytic Decomposition of Ozone: Hausmannite Mn_3O_4 on Exposed (101) Crystal Surface. *J. Hazard. Mater.* **2023**, *458*, 131947.
(31) Zhu, W.-D.; Wang, C.-W.; Chen, J.-B.; Li, Y.; Wang, J. Enhanced Field Emission from Ti^{3+} Self-doped TiO_2 Nanotube Arrays Synthesized by a Facile Cathodic Reduction Process. *Appl. Surf. Sci.* **2014**, *301*, 525−529.
(32) Naldoni, A.; Allieta, M.; Santangelo, S.; Marelli, M.; Fabbri, F.; Cappelli, S.; Bianchi, C. L.; Psaro, R.; Dal Santo, V. Effect of Nature and Location of Defects on Bandgap Narrowing in Black TiO_2 Nanoparticles. *J. Am. Chem. Soc.* **2012**, *134* (18), 7600−7603.
(33) Dai, W.; Zhang, B.; Ji, J.; Liu, B.; Xie, R.; Gan, Y.; Xie, X.; Zhang, J.; Huang, P.; Huang, H. Exceptional Ozone Decomposition over δ-MnO_2/AC under an Entire Humidity Environment. *Environ. Sci. Technol.* **2023**, *57*, 17727−17736.
(34) Dai, W.; Zhang, B.; Ji, J.; Zhu, T.; Liu, B.; Gan, Y.; Xiao, F.; Zhang, J.; Huang, H. Efficient Ozone Elimination Over MnO_2 via Double Moisture-Resistance Protection of Active Carbon and CeO_2. *Environ. Sci. Technol.* **2024**, *58* (27), 12091−12100.
(35) Qiu, L.; Zhang, F.; Qian, Y.; Han, W.; He, Y.; Feng, X.; Jin, J.; Gu, Y.; Hao, S.; Zhang, X. Europium Doped RuO_2@TP Enhanced Chlorine Evolution Reaction Performance by Charge Redistribution. *Chem. Eng. J.* **2023**, *464*, 142623.
(36) Han, W.; Qian, Y.; Zhang, F.; He, Y.; Li, P.; Zhang, X. Ultrasmall IrO_2 Nanoparticles Anchored on Hollow Co-Mo Multi-oxide Heterostructure Nanocages for Efficient Oxygen Evolution in Acid. *Chem. Eng. J.* **2023**, *473*, 145353.
(37) Han, W.; Zhang, F.; Qiu, L.; Qian, Y.; Hao, S.; Li, P.; He, Y.; Zhang, X. Interface Engineering of Hierarchical NiCoP/$NiCoS_x$ Heterostructure Arrays for Efficient Alkaline Hydrogen Evolution at Large Current Density. *Nanoscale* **2022**, *14* (41), 15498−15506.
(38) Zhang, F.; Wang, X.; Han, W.; Qian, Y.; Qiu, L.; He, Y.; Lei, L.; Zhang, X. The Synergistic Activation of Ce Doping and CoP/Ni_3P Hybrid Interaction for Efficient Water Splitting at Large Current Density. *Adv. Funct. Mater.* **2023**, *33* (9), 2212381.
(39) Du, H.; Wang, T.; He, S.; Li, B.; Wang, K.; Chen, Q.; Du, Z.; Ai, W.; Huang, W. Mountain Shaped Nickel Nanostripes Enabled by Facet Engineering of Nickel Foam: A New Platform for High Current Density Water Splitting. *Adv. Funct. Mater.* **2024**, *34* (14), 2311854.
(40) Wu, T.; Song, E.; Zhang, S.; Luo, M.; Zhao, C.; Zhao, W.; Liu, J.; Huang, F. Engineering Metallic Heterostructure Based on Ni_3N and 2M MoS_2 for Alkaline Water Electrolysis with Industry Compatible Current Density and Stability. *Adv. Mater.* **2022**, *34* (9), 2108505.
(41) Cheng, Y.; Fu, P.; Yu, Z.; Yang, X.; Zhang, Y.; Yuan, A.; Liu, H.; Du, J.; Chen, L. Modulation of the Multiphase Phosphorus/sulfide Heterogeneous Interface via Rare Earth for Solar enhanced Water Splitting at Industrial level Current Densities. *Carbon Neutralization* **2024**, *3*, 873.
(42) Zhang, L.; Hu, M.; Li, H.; Cao, B.; Jing, P.; Liu, B.; Gao, R.; Zhang, J.; Liu, B. Boosting Hydrogen Evolution Reaction via Electronic Coupling of Cerium Phosphate with Molybdenum Phosphide Nanobelts. *Small* **2021**, *17* (40), 2102413.
(43) Li, J. F.; Huang, Y. F.; Ding, Y.; Yang, Z. L.; Li, S. B.; Zhou, X. S.; Fan, F. R.; Zhang, W.; Zhou, Z. Y.; Wu, D. Y.; Ren, B.; Wang, Z. L.; Tian, Z. Q. Shell-isolated Nanoparticle-enhanced Raman Spectroscopy. *Nature* **2010**, *464* (7287), 392−395.
(44) Ni, B.; Shen, P.; Zhang, G.; Zhao, J.; Ding, H.; Ye, Y.; Yue, Z.; Yang, H.; Wei, H.; Jiang, K. Second-Shell N Dopants Regulate Acidic O_2 Reduction Pathways on Isolated Pt Sites. *J. Am. Chem. Soc.* **2024**, 11181−11192.
(45) Zhao, J.; Lian, J.; Zhao, Z.; Wang, X.; Zhang, J. A Review of In-Situ Techniques for Probing Active Sites and Mechanisms of Electrocatalytic Oxygen Reduction Reactions. *Nano-Micro Lett.* **2023**, *15* (1), 19.
(46) Wren, J. C.; Paquette, J.; Sunder, S.; Ford, B. L. Iodine chemistry in the + 1 oxidation state. II. A Raman and Uv-visible Spectroscopic Study of the Disproportionation of Hypoiodite in Basic Solutions. *Can. J. Chem.* **1986**, *64*, 2284−2296.
(47) Chen, S.; Wang, H.; Kang, Z.; Jin, S.; Zhang, X.; Zheng, X.; Qi, Z.; Zhu, J.; Pan, B.; Xie, Y. Oxygen Vacancy Associated Single-electron Transfer for Photofixation of CO_2 to Long-chain Chemicals. *Nat. Commun.* **2019**, *10* (1), 788.
(48) Guo, S.; Heck, K.; Kasiraju, S.; Qian, H.; Zhao, Z.; Grabow, L. C.; Miller, J. T.; Wong, M. S. Insights into Nitrate Reduction over Indium-Decorated Palladium Nanoparticle Catalysts. *ACS Catal.* **2018**, *8* (1), 503−515.
(49) Xu, H.; Cheng, D.; Cao, D.; Zeng, X. C. A Universal Principle for a Rational Design of Single-atom Electrocatalysts. *Nat. Catal.* **2018**, *1* (5), 339−348.

https://doi.org/10.1021/cbe.4c00187
Chem Bio Eng. 2025, 2, 322−331